

## Supplementary Materials for

# Multimodal contrastive learning for spatial gene expression prediction using histology images

### Supplementary Notes

#### 1. Key contributions of the paper

In this paper, we propose mclSTExp, a multimodal deep learning approach utilizing Transformer and contrastive learning architecture. The key contributions of the paper can be summarized as follows:

- In this study, we propose a multimodal deep learning approach based on Transformer and contrastive learning framework, aiming to integrate spot features, spatial location information of spots, and H&E image data for predicting spatial gene expression from H&E images.
- Utilizing the unique characteristics of ST data, particularly gene spatial location information, we treat spots as “words” and spot sequences as “sentences” containing multiple “words”. We employ a self-attention mechanism within the Transformer encoder of mclSTExp to extract spot features, and seamlessly integrate this information using learnable positional encoding.
- We infer gene expression profiles through weighted aggregation, rather than simple averaging, akin to using the softmax function.
- Our method was compared with competing approaches on multiple real ST datasets. The results demonstrate that our method achieves a 23% to 36% improvement in predicting gene expression profiles in terms of average Pearson Correlation Coefficient (PCC) compared to the state-of-the-art methods. Additionally, our approach not only demonstrates higher accuracy in interpreting cancer-specific genes, elucidating immune-related genes, and identifying specific spatial domains, but also preserves the original gene expression patterns, thereby providing valuable insights for cancer therapy.

#### 2. Dataset description and data preprocessing

The proposed mclSTExp and competing methods are evaluated on three real datasets (Table S1). Each dataset includes H&E images, spatial gene expression data, and spot coordinates as follows:

- The lower resolution (100  $\mu\text{m}$  per spot) **HER2+** dataset [1] contains 36 tissue sections obtained from eight patients. We selected and retained 32 sections from seven patients, ensuring that each section had a minimum of 180 spots.
- The lower resolution (100  $\mu\text{m}$  per spot) **cSCC** dataset [2] contains 12 tissue sections obtained from four patients, with each patient contributing three sections.
- The higher resolution (55  $\mu\text{m}$  per spot) **Alex+10x** dataset contains of 9 breast cancer tissue samples, including 3 samples (2 fresh-frozen and 1 formalin-fixed-paraffin-embedded, FFPE, tissue) from 10x Genomics [3] and six samples obtained from Swarbrick’s laboratory [4].

For H&E images, we partitioned a  $W \times H$  pixel region around each sequencing spot based on its positional coordinates, where  $W$  and  $H$  denote the width and height of the patches, respectively. Both  $W$  and  $H$  are set to 224, corresponding to the diameter of each spot in the ST data.

For the spatial gene expression data, we initially identify common genes across all tissue sections in the training ST data. Subsequently, we choose the top 1,000 highly variable genes (HVG) in each tissue section, excluding genes expressed in fewer than 1,000 spots across all tissue sections. The counts for each spot were normalized by dividing the total counts for that spot and then scaled by a factor of 1,000,000. Finally, the values are transformed to a natural log scale, i.e.,  $\log(x + 1)$ .

After pre-processing the ST datasets, HER2+ retained 11,548 spots with 785 genes, cSCC retained 8,671 spots with 171 genes, and Alex+10x retained 25,914 spots with 685 genes, as detailed in Table S1. We paired image patches with spots, resulting in  $N^2$  squared samples of (patches, spot) pairs. Since the patches are divided based on the positional coordinates of the spots, spots and patches with the same positional coordinates naturally form positive sample pairs. Among these, there are  $N$  positive samples, representing correctly matched (patches, spot) pairs, and the remaining  $N^2 - N$  samples are negative instances, representing incorrectly matched (patches, spot) pairs. To evaluate the predictive accuracy of gene expression data, we employed a leave-one-out cross-validation training approach, where one tissue slice was held out as the test set, and the remaining slices were utilized as the training set.

Leave-one-out cross-validation is a specific cross-validation technique used to evaluate the performance of machine learning models. Specifically, each time, all data except one sample are used for training, and the single remaining sample is used for validation. This process is repeated until every sample has been used once as a validation set. This approach ensures that each sample is systematically used as a validation set, providing a comprehensive and accurate assessment of the model’s performance.

#### 3. Details on comparison with other gene expression prediction methods

In this study, we selected five representative state-of-the-art methods:

- **STnet** [5] utilized DenseNet-121 as the image encoder to extract H&E image features, which were then embedded into the feature space and projected onto the dimension of gene expression through fully connected layers.

- **HisToGene** [1] adopted a vision Transformer as the image encoder, leveraging self-attention mechanism to extract global features, which were subsequently projected onto the dimension of gene expression through fully connected layers.
- **His2ST** [6] employed the Convmixer module to capture the internal relationships of 2D visual features within H&E images through convolution operations. Additionally, the Transformer module captured global spatial dependencies using a self-attention mechanism, while the GNN module explicitly captured the neighborhood relationships between spots.
- **THItogene** [7] used H&E images as input and employed dynamic convolutional and capsule networks to capture signals of potential molecular features within histological samples.
- **BLEEP** [8] utilized a contrastive learning approach, introducing image and gene expression encoders to jointly learn embeddings in feature space for inferring gene expression.

#### 4. Experiment settings

We employed a grid search strategy to systematically explore the combinations of hyperparameters. Each combination was evaluated based on performance metrics on the validation set. For instance, we tested a range of learning rates [1e-5, 1e-4, 1e-3, 1e-2] to identify the optimal value that ensures stable convergence. Additionally, we experimented with various embedding dimensions [128, 256, 512, 1024] to determine the dimensionality that captures the most relevant features while maintaining computational efficiency. Regularization was performed using different weight decay values [0.0001, 0.001, 0.01, 0.1] to prevent overfitting.

mclSTExp is trained from scratch for 90 epochs on the HER2+, cSCC datasets, and 15 epochs on the Alex+10x dataset. A batch size of 128 was used during training. The learning rate was set to  $1 \times 10^{-4}$ , and the weight decay was  $1 \times 10^{-3}$ . All experiments are conducted using NVIDIA RTX 4090 GPUs with the AdamW optimizer.

In mclSTExp, a two-layer Transformer is employed as the spot encoder, with 8 attention heads, each with a dimensionality of 64. Additionally, within the contrastive learning module, the temperature hyperparameter was set to 1, and the dimensionality of the multimodal embedding space was specified as 256.

#### 5. Evaluation criteria

We use PCC, Mean Squared Error (MSE), and Mean Absolute Error (MAE) to evaluate the proposed method against baselines.

$$\text{PCC} = \frac{\text{Cov}(X_{\text{observed}}, X_{\text{pred}})}{\text{Var}(X_{\text{observed}}) \times \text{Var}(X_{\text{pred}})}, \quad (1)$$

where  $\text{Cov}()$  is the covariance, and  $\text{Var}()$  is the variance.  $X_{\text{observed}}$  and  $X_{\text{pred}}$  are the observed and predicted gene expression, respectively.

$$\text{MSE} = \frac{1}{N} \sum_{i=1}^N (X_{\text{observed}} - X_{\text{pred}})^2, \quad (2)$$

$$\text{MAE} = \frac{1}{N} \sum_{i=1}^N |X_{\text{observed}} - X_{\text{pred}}|, \quad (3)$$

PCC measures the mean correlation for each gene type, considering predictions and ground truth across all slide images. Meanwhile, MSE and MAE measure the sample deviation between predictions and ground truth for each gene type in each slide image. For PCC, a higher value indicates better performance. Conversely, for MSE and MAE, lower values indicate better performance.

In the assessment of spatial clustering performance, we employ the Adjusted Rand Index (ARI) to measure the correlation between the clustering outcomes and the actual pathological annotation regions. The ARI can be mathematically expressed as follows:

$$\text{ARI} = \frac{\sum_{ij} \binom{n_{ij}}{2} - \frac{[\sum_i \binom{a_i}{2} \sum_j \binom{b_j}{2}]}{\binom{n}{2}}}{\frac{1}{2} [\sum_i \binom{a_i}{2} + \sum_j \binom{b_j}{2}] - \frac{[\sum_i \binom{a_i}{2} \sum_j \binom{b_j}{2}]}{\binom{n}{2}}}, \quad (4)$$

where  $a_i$  and  $b_j$  are the number of samples appearing in the  $i$ -th predicted cluster and the  $j$ -th true cluster, respectively.  $n_{ij}$  means the number of overlaps between the  $i$ -th predicted cluster and the  $j$ -th true cluster. The ARI is a metric with a scale ranging from -1 to 1. A value nearing 1 signifies a stronger alignment between the clustering results and the true labels.

Additionally, the Normalized Mutual Information (NMI) is another measure utilized for evaluating clustering performance, defined as:

$$\text{NMI} = \frac{I(X; Y)}{\sqrt{H(X) \cdot H(Y)}}. \quad (5)$$

where  $I(X; Y)$  denotes the mutual information between the predicted clustering  $X$  and the true clustering  $Y$ , and  $H(X)$  and  $H(Y)$  represent the entropies of  $X$  and  $Y$ , respectively.

#### 6. Spatial region detection

To evaluate the performance of various methods in identifying specific spatial domains on entire H&E images, we compared six tissue slices from the HER2+ dataset. These slices have been annotated by pathologists for spatial transcriptomic analysis. Initially, we employed PCA dimensionality reduction on the predicted data from mclSTExp, followed by Kmeans clustering. Compared to other methods, mclSTExp demonstrates the ability to accurately identify spatial domains predefined by pathologists, resulting in significant improvements in effectiveness. As shown in Figure S3, our method achieved the highest ARI and NMI scores across

all slices. Specifically, mclSTExp (avg  $ARI = 0.2646$ , avg  $NMI = 0.2853$ ) outperforms the second-ranked method, His2ST (avg  $ARI = 0.1647$ , avg  $NMI = 0.2088$ ), by 60.7% in terms of average ARI and by 36.6% in terms of average NMI. For the B1 slice, mclSTExp ( $ARI = 0.381$ ,  $NMI = 0.429$ ) achieves similar ARI and NMI scores as His2ST ( $ARI = 0.354$ ,  $NMI = 0.417$ ). However, for the E1 and F1 slices, mclSTExp accurately identifies their spatial structures, whereas all other methods perform poorly.

Compared to existing methods, mclSTExp treats each spot as a “word” and spot sequences as “sentences”, integrating the features and positional information of each spot through a self-attention mechanism. Additionally, by incorporating H&E image information through contrastive learning, mclSTExp learns rich representations, enabling it to sensitively capture subtle differences in H&E images, as well as the correlation between H&E images and gene expression, along with abundant spatial information. Consequently, gene expression data predicted by mclSTExp demonstrate superior performance in identifying spatial domains and better reflect the true spatial structure and biological characteristics of tissues.

## 7. Ablation studies

To assess the contribution of each module in our proposed mclSTExp model, we conducted a detailed ablation studies on the ST dataset.

We first conducted the ablation studies on positional encodings (Table S4). We compared the performance impact of different positional encoding methods on the HER2+, cSCC, and Alex+10x datasets. The results indicate that employing learnable positional encoding methods (learnable PE) consistently yielded the best performance across all datasets. Compared to other positional encoding methods, including no encoding, sinusoidal encoding, and naive encoding, learnable PE achieved lower PCC (ACG) and PCC (HEG) scores, as well as higher MSE and MAE scores. This suggests that adopting learnable positional encoding methods better captures the spatial information of spots, thereby improving model performance in ST analysis. Particularly, on the Alex+10x dataset, using learnable PE resulted in a 15.18% improvement in ACG and a 6.65% improvement in PCC (HEG) prediction accuracy compared to not using positional encoding. This indicates that without the fusion of positional information, the model may struggle to fully utilize the positional information of spots, potentially leading to insufficient understanding of spatial structures and affecting the model’s ability to model the data. In contrast, incorporating positional information fusion enables a more accurate understanding of spatial features, thereby enhancing model generalization and performance. Therefore, in ST analysis, integrating positional information fusion is essential and effective.

Furthermore, we conducted the ablation studies of the image encoder on three different datasets, namely HER2+, cSCC, and Alex+10x (Table S5). The results indicate that Denesnet121 outperforms pre-trained ViT and ResNet50 across all evaluation metrics (Table S5).

Lastly, we conducted the ablation studies on distance metrics. Three different distance metrics, including L1 norm, cosine similarity, and L2 norm, were compared across the HER2+, cSCC, and Alex+10x datasets (Table S6). On the HER2+ dataset, the L2 norm method exhibited the best performance across all evaluation metrics, including PCC (ACG), PCC (HEG), MSE, and MAE, with average values of 0.2306, 0.3878, 0.6007, and 0.5868, respectively. Similarly, on the cSCC dataset and Alex+10x dataset, the L2 norm method also demonstrated superior performance, indicating its advantage in distance measurement. These findings suggest that, for these three datasets, the L2 norm, as a distance metric method, can better capture the relationships between gene expressions, thereby improving the accuracy of gene expression prediction.

We also conducted a sensitivity analysis on the top- $k$  parameter, as illustrated in Figure S4. On both the HER2+ and cSCC datasets, mclSTExp achieved the highest PCC and the lowest MAE and MSE with  $k = 200$  for all considered genes. Similarly, on the Alex+10x dataset, mclSTExp attained the highest PCC and the lowest MAE and MSE with  $k = 2400$  for all considered genes.

To better explore the impact of different parameterized versions of the loss function on experimental results, we organized an ablation study on a parameterized version of the loss function. Specifically, for the loss function, we investigated the effect of the parameter  $\lambda$  when it is set to 0, 1, and 0.5, which is detailed in Table S7 of the supplementary materials. We found that the performance difference between  $\lambda = 0$  and  $\lambda = 1$  was minimal. However, using the mean of both loss functions ( $\lambda = 0.5$ ) resulted in improved overall performance.

## 8. Code Availability

All source codes used in our experiments have been deposited at <https://github.com/shizhiceng/mclSTExp>.

## 9. Data Availability

Three publicly available ST datasets were used in this study (Table S1), which can be found : (1) human HER2-positive breast tumor ST data from <https://github.com/almaan/her2st/>. (2) human cutaneous squamous cell carcinoma 10x Visium data from GSE144240. (3) 10x Genomics Visium data and Swarbrick’s Laboratory Visium data from <https://doi.org/10.48610/4fb74a9>.

## Supplementary Figures



**Figure S1.** Visualization of the cSCC dataset by the top seven predicted genes with the highest values of average  $-\log_{10}$  p-values across all tissue sections, where the p-value for each tissue section was obtained according to the correlation between the predicted and observed gene expression. For each of the seven genes, the tissue section that had the smallest p-value by our model was selected for visualization.

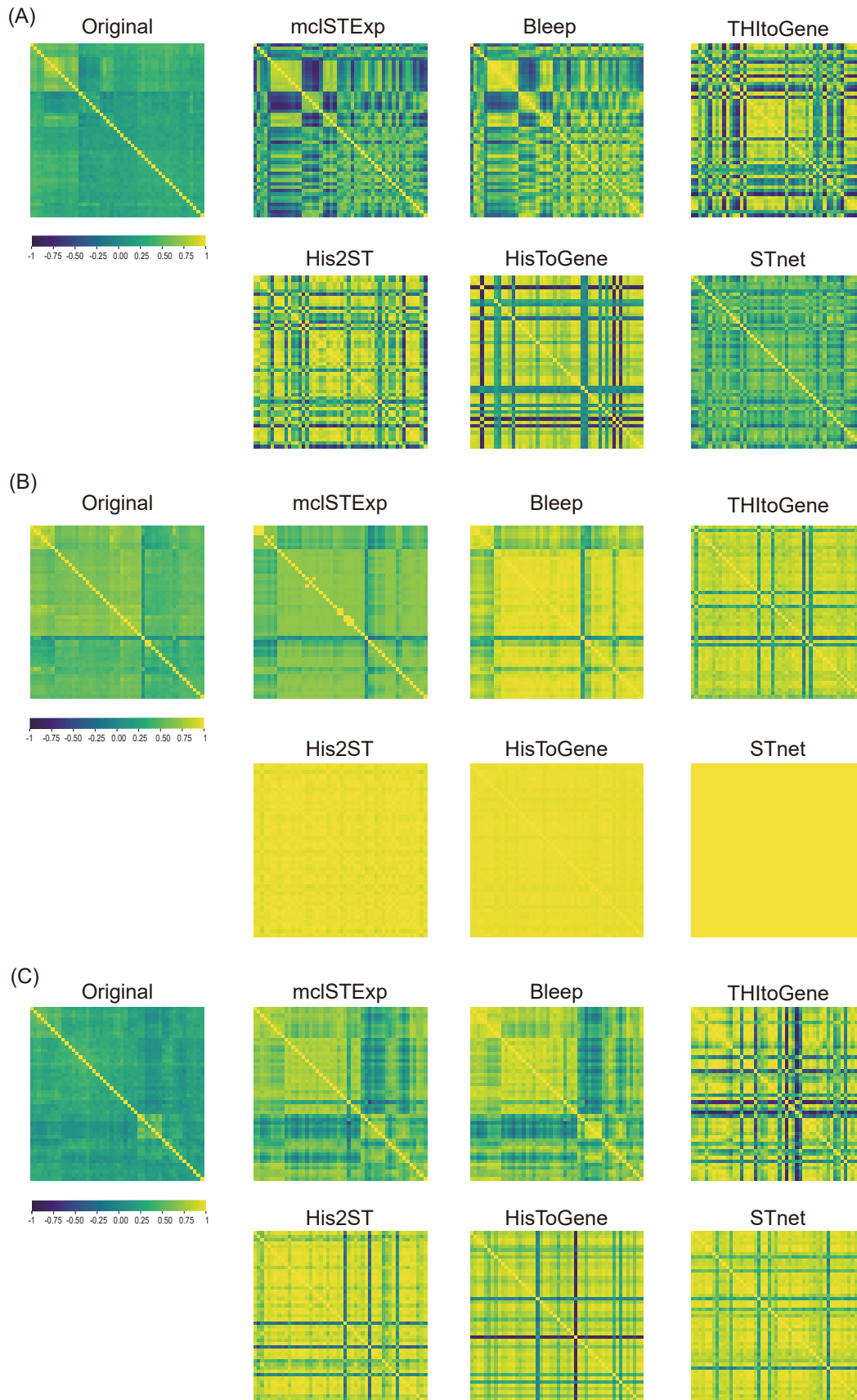


**Figure S2.** (A), (B), and (C) respectively represent the gene-gene correlation heatmaps calculated using the predicted expressions for the HER2+, cSCC, and Alex+10x datasets. It illustrates the effectiveness of mclSTExp in preserving gene-gene correlations, serving as evidence of its capability to maintain relevant biological heterogeneity.



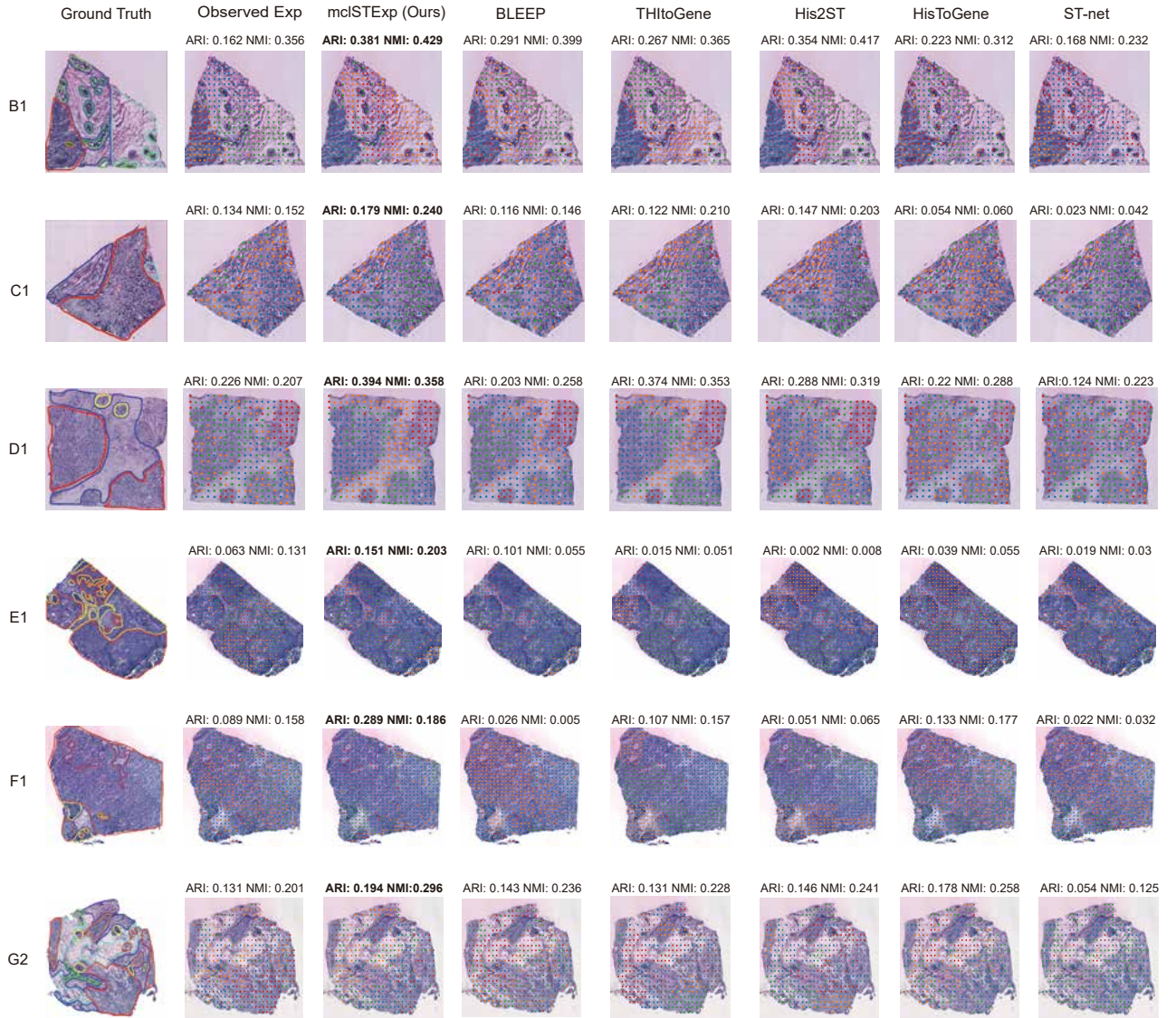


**Figure S3.** We conducted spatial clustering analysis using six H&E images annotated by pathologists from the HER2+ dataset, while “Observed Exp” represents clustering directly using the sequenced gene expression.

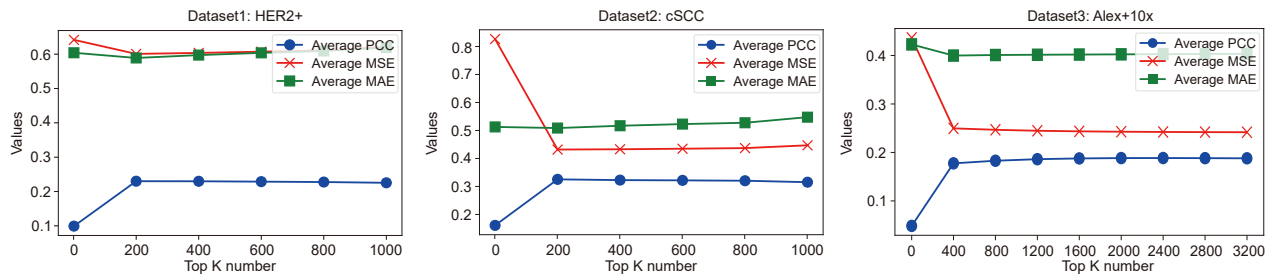


**Figure S4.** Ablation studies of the parameter  $k$  of mclSTExp on the HER2+, cSCC and Alex+10x datasets. The PCC, MSE, and MAE were calculated between the gene expression data predicted by mclSTExp for all considered genes (ACG) and the observed data.

## Supplementary Tables

**Table S1.** Summary of the preprocessed datasets.

Dataset	H&E images	Resolution	Spots	Genes
HER2+ [1]	32	100 $\mu\text{m}$	11548	785
cSCC [2]	12	100 $\mu\text{m}$	8671	171
Alex+10x [3, 4]	9	55 $\mu\text{m}$	25914	685

**Table S2.** The top 50 predicted genes by mclSTExp were ranked based on the highest values of mean  $-\log_{10}$  p-values across all tissue sections in the HER2+ dataset, where the p-value for each tissue section was obtained according to the correlation between the predicted and observed gene expression.

Rank	Gene	Average $-\log_{10}$ p-values	Rank	Gene	Average $-\log_{10}$ p-values
1	GNAS	31.7374979	26	TMBIM6	15.60088382
2	FN1	29.48300509	27	CCT4	15.48815636
3	FASN	26.5014407	28	C3	15.39573578
4	HLA-B	23.81602936	29	MUC1	15.31770172
5	SCD	23.38638176	30	MUCL1	15.30780106
6	IGKC	22.89352328	31	PRKCSH	15.29308679
7	HLA-DRA	21.18646565	32	BSG	15.21926999
8	CD74	20.83984843	33	NDUFB9	14.92890652
9	CLDN4	20.56337901	34	NDUFB2	14.89028399
10	UBA52	19.82961524	35	KRT8	14.87707216
11	HSPB1	19.37419648	36	FLNA	14.8221481
12	MYL12B	19.36653237	37	GPRC5A	14.79007249
13	STMN1	18.21896248	38	FADS2	14.76694248
14	IGLC3	17.95928677	39	LUM	14.60046262
15	IGHA1	17.82911851	40	HMGB2	14.59822067
16	IGLC2	17.82198295	41	TIMP1	14.597522
17	RHOB	17.58603295	42	AES	14.5492234
18	IGHG3	17.44433543	43	CRACR2B	14.40019307
19	VIM	17.41394217	44	POSTN	14.38532508
20	TMEM123	17.27330474	45	ITGB6	14.26458071
21	SPARC	16.66613648	46	HLA-DPA1	14.2525189
22	CLDN3	16.66542256	47	IGHM	14.20466249
23	COL3A1	16.57054216	48	ATP6AP1	14.14672836
24	CRABP2	16.19007526	49	TXNDC17	14.012606
25	NDRG1	41.05857062	50	S100A14	13.9632133

**Table S3.** The top 50 predicted genes by mclSTExp were ranked based on the highest values of mean  $-\log_{10}$  p-values across all tissue sections in the cSCC dataset, where the p-value for each tissue section was obtained according to the correlation between the predicted and observed gene expression

Rank	Gene	Average $-\log_{10}$ p-values	Rank	Gene	Average $-\log_{10}$ p-values
1	RPL13	95.16443206	26	NEFL	40.50223942
2	SBSN	87.44024527	27	CASP14	40.48121358
3	DMKN	84.14861043	28	TMOD3	38.87176597
4	ANXA1	81.22854158	29	EIF5	38.8020682
5	NDRG1	79.75989866	30	MOB1A	37.78479111
6	KRTDAP	78.30615159	31	IGFL1	37.32555753
7	SPRR2A	73.20378609	32	KLF6	37.28006497
8	PI3	66.80329099	33	KIF5B	35.71358568
9	HSP90AA1	66.36587578	34	PTP4A2	35.62163211
10	ITGA6	65.53533137	35	PAICS	35.34727207
11	CALML5	61.98991283	36	STMN1	35.25029249
12	SPINK5	60.09701412	37	NAP1L1	35.12576686
13	COL1A2	54.46153265	38	PRRC2C	35.10933098
14	MSMO1	52.8260604	39	WNK1	34.9209555
15	SPRR2D	52.11175327	40	CYFIP1	34.50573809
16	ACTN4	48.61148361	41	PTHLH	34.32614153
17	HSPH1	46.36376299	42	CTNND1	34.28747832
18	ENAH	46.10806832	43	CAV1	33.40027545
19	COL3A1	45.35231055	44	RALA	31.60494295
20	FDFT1	44.67386954	45	F3	31.44476584
21	PSMA7	43.34262318	46	DIAPH1	31.32501815
22	MAFB	42.1321182	47	DDX21	31.26470445
23	EFNB1	41.69393662	48	SRP72	31.04323875
24	ZFP36L2	41.18945052	49	EIF5B	30.96488263
25	NHP2	41.05857062	50	PSMD1	30.79251656



**Table S4.** Ablation studies of positional encoding methods across the HER2+, cSCC, and Alex+10x datasets.

Position Encoding Methods	HER2+			
	PCC (ACG)	PCC (HEG)	MSE	MAE
W/O	$0.2105 \pm 0.009$	$0.3578 \pm 0.012$	$0.6220 \pm 0.008$	$0.6323 \pm 0.006$
Sinusiod PE [9]	$0.2184 \pm 0.013$	$0.3728 \pm 0.015$	$0.6596 \pm 0.007$	$0.6795 \pm 0.014$
Naive PE [10]	$0.2262 \pm 0.011$	$0.3796 \pm 0.007$	$0.6162 \pm 0.014$	$0.5975 \pm 0.008$
<b>learnable PE [11]</b>	<b><math>0.2322 \pm 0.016</math></b>	<b><math>0.3923 \pm 0.018</math></b>	<b><math>0.5815 \pm 0.011</math></b>	<b><math>0.5714 \pm 0.013</math></b>
Position Encoding Methods	cSCC			
	PCC (ACG)	PCC (HEG)	MSE	MAE
W/O	$0.3089 \pm 0.014$	$0.4164 \pm 0.011$	$0.4467 \pm 0.008$	$0.5172 \pm 0.007$
Sinusiod PE [9]	$0.3125 \pm 0.011$	$0.4171 \pm 0.014$	$0.4439 \pm 0.012$	$0.5191 \pm 0.005$
Naive PE [10]	$0.3217 \pm 0.013$	$0.4230 \pm 0.009$	$0.4344 \pm 0.011$	$0.5123 \pm 0.012$
<b>learnable PE [11]</b>	<b><math>0.3235 \pm 0.016</math></b>	<b><math>0.4259 \pm 0.010</math></b>	<b><math>0.4302 \pm 0.012</math></b>	<b><math>0.5058 \pm 0.014</math></b>
Position Encoding Methods	Alex+10x			
	PCC (ACG)	PCC (HEG)	MSE	MAE
W/O	$0.1692 \pm 0.020$	$0.3379 \pm 0.013$	$0.2510 \pm 0.008$	$0.3987 \pm 0.011$
Sinusiod PE [9]	$0.1789 \pm 0.013$	$0.3508 \pm 0.015$	$0.2424 \pm 0.009$	$0.4088 \pm 0.013$
Naive PE [10]	$0.1795 \pm 0.015$	$0.3496 \pm 0.014$	$0.2398 \pm 0.014$	$0.3961 \pm 0.005$
<b>learnable PE [11]</b>	<b><math>0.1949 \pm 0.018</math></b>	<b><math>0.3604 \pm 0.013</math></b>	<b><math>0.2394 \pm 0.011</math></b>	<b><math>0.3897 \pm 0.009</math></b>

**Table S5.** Ablation studies of image encoders on the HER2+, cSCC and Alex+10x datasets.

Image Encoders	HER2+			
	PCC (ACG)	PCC (HEG)	MSE	MAE
ViT	$0.2236 \pm 0.009$	$0.3750 \pm 0.004$	$0.6007 \pm 0.005$	$0.5853 \pm 0.008$
Resnet50	$0.2298 \pm 0.003$	$0.3889 \pm 0.007$	$0.6058 \pm 0.006$	$0.5878 \pm 0.005$
<b>Denesnet121</b>	<b><math>0.2312 \pm 0.004</math></b>	<b><math>0.3923 \pm 0.008</math></b>	<b><math>0.5821 \pm 0.004</math></b>	<b><math>0.5714 \pm 0.004</math></b>
Image Encoder	cSCC			
	PCC (ACG)	PCC (HEG)	MSE	MAE
ViT	$0.2994 \pm 0.007$	$0.3996 \pm 0.006$	$0.4485 \pm 0.007$	$0.5232 \pm 0.009$
Resnet50	$0.3113 \pm 0.005$	$0.4139 \pm 0.005$	$0.4385 \pm 0.004$	$0.5195 \pm 0.008$
<b>Denesnet121</b>	<b><math>0.3235 \pm 0.010</math></b>	<b><math>0.4249 \pm 0.009</math></b>	<b><math>0.4302 \pm 0.006</math></b>	<b><math>0.5058 \pm 0.005</math></b>
Image Encoder	Alex+10x			
	PCC (ACG)	PCC (HEG)	MSE	MAE
ViT	$0.1745 \pm 0.012$	$0.3023 \pm 0.011$	$0.2724 \pm 0.007$	$0.4454 \pm 0.008$
Resnet50	$0.1801 \pm 0.009$	$0.3228 \pm 0.010$	$0.2394 \pm 0.008$	$0.4019 \pm 0.006$
<b>Denesnet121</b>	<b><math>0.1948 \pm 0.011</math></b>	<b><math>0.3511 \pm 0.008</math></b>	<b><math>0.2373 \pm 0.006</math></b>	<b><math>0.3997 \pm 0.009</math></b>

**Table S6.** Ablation studies of distance metrics on the HER2+, cSCC and Alex+10x datasets.

Distance	HER2+			
	PCC (ACG)	PCC (HEG)	MSE	MAE
cosine	$0.2301 \pm 0.002$	$0.3871 \pm 0.007$	$0.6009 \pm 0.009$	$0.5889 \pm 0.008$
L1	$0.2300 \pm 0.005$	$0.3872 \pm 0.004$	$0.5963 \pm 0.007$	$0.5901 \pm 0.004$
<b>L2</b>	<b><math>0.2306 \pm 0.004</math></b>	<b><math>0.3878 \pm 0.018</math></b>	<b><math>0.5811 \pm 0.006</math></b>	<b><math>0.5868 \pm 0.003</math></b>
distance	cSCC			
	PCC (ACG)	PCC (HEG)	MSE	MAE
cosine	$0.3262 \pm 0.004$	$0.4124 \pm 0.005$	$0.4317 \pm 0.007$	$0.5063 \pm 0.008$
L1	$0.3184 \pm 0.003$	$0.4098 \pm 0.006$	$0.4320 \pm 0.007$	$0.5061 \pm 0.007$
<b>L2</b>	<b><math>0.3322 \pm 0.007</math></b>	<b><math>0.4261 \pm 0.009</math></b>	<b><math>0.4302 \pm 0.005</math></b>	<b><math>0.5058 \pm 0.006</math></b>
distance	Alex+10x			
	PCC (ACG)	PCC (HEG)	MSE	MAE
cosine	$0.2262 \pm 0.011$	$0.3596 \pm 0.007$	$0.6162 \pm 0.014$	$0.5975 \pm 0.008$
L1	$0.2184 \pm 0.013$	$0.3528 \pm 0.015$	$0.6596 \pm 0.007$	$0.6795 \pm 0.014$
<b>L2</b>	<b><math>0.1948 \pm 0.016</math></b>	<b><math>0.3623 \pm 0.018</math></b>	<b><math>0.2394 \pm 0.011</math></b>	<b><math>0.3997 \pm 0.013</math></b>

**Table S7.** Ablation studies on a parameterized version of the loss function for the HER2+, cSCC, and Alex+10x datasets.

$\lambda \times \text{loss\_image} + (1-\lambda) \times \text{loss\_spot}$	HER2+			
	<u>PCC(ACG)</u>	<u>PCC(HEG)</u>	<u>MSE</u>	<u>MAE</u>
<u><math>\lambda = 0</math></u>	<u><math>0.2251 \pm 0.010</math></u>	<u><math>0.3805 \pm 0.014</math></u>	<u><math>0.5974 \pm 0.012</math></u>	<u><math>0.5983 \pm 0.011</math></u>
<u><math>\lambda = 1</math></u>	<u><math>0.2211 \pm 0.011</math></u>	<u><math>0.3789 \pm 0.013</math></u>	<u><math>0.6014 \pm 0.011</math></u>	<u><math>0.5948 \pm 0.015</math></u>
<u><math>\lambda = 0.5</math></u>	<b><u><math>0.2309 \pm 0.006</math></u></b>	<b><u><math>0.3891 \pm 0.011</math></u></b>	<b><u><math>0.5891 \pm 0.015</math></u></b>	<b><u><math>0.5864 \pm 0.013</math></u></b>
$\lambda \times \text{loss\_image} + (1-\lambda) \times \text{loss\_spot}$	cSCC			
	<u>PCC(ACG)</u>	<u>PCC(HEG)</u>	<u>MSE</u>	<u>MAE</u>
<u><math>\lambda = 0</math></u>	<u><math>0.3177 \pm 0.021</math></u>	<u><math>0.4162 \pm 0.013</math></u>	<u><math>0.4418 \pm 0.011</math></u>	<u><math>0.5319 \pm 0.012</math></u>
<u><math>\lambda = 1</math></u>	<u><math>0.3248 \pm 0.017</math></u>	<u><math>0.4275 \pm 0.014</math></u>	<u><math>0.4521 \pm 0.010</math></u>	<u><math>0.5594 \pm 0.014</math></u>
<u><math>\lambda = 0.5</math></u>	<b><u><math>0.3294 \pm 0.015</math></u></b>	<b><u><math>0.4281 \pm 0.016</math></u></b>	<b><u><math>0.4302 \pm 0.010</math></u></b>	<b><u><math>0.5208 \pm 0.009</math></u></b>
$\lambda \times \text{loss\_image} + (1-\lambda) \times \text{loss\_spot}$	Alex+10x			
	<u>PCC(ACG)</u>	<u>PCC(HEG)</u>	<u>MSE</u>	<u>MAE</u>
<u><math>\lambda = 0</math></u>	<u><math>0.1755 \pm 0.007</math></u>	<u><math>0.3464 \pm 0.015</math></u>	<u><math>0.2402 \pm 0.010</math></u>	<u><math>0.3992 \pm 0.013</math></u>
<u><math>\lambda = 1</math></u>	<u><math>0.1879 \pm 0.009</math></u>	<u><math>0.3510 \pm 0.013</math></u>	<u><math>0.2469 \pm 0.009</math></u>	<u><math>0.4123 \pm 0.014</math></u>
<u><math>\lambda = 0.5</math></u>	<b><u><math>0.1948 \pm 0.011</math></u></b>	<b><u><math>0.3611 \pm 0.018</math></u></b>	<b><u><math>0.2329 \pm 0.006</math></u></b>	<b><u><math>0.3897 \pm 0.011</math></u></b>

## References

1. Minxing Pang, Kenong Su, and Mingyao Li. Leveraging information in spatial transcriptomics to predict super-resolution gene expression from histology images in tumors. *BioRxiv*, pages 1–31, 2021.
2. Andrew L Ji, Adam J Rubin, Kim Thrane, Sizun Jiang, David L Reynolds, Robin M Meyers, Margaret G Guo, Benson M George, Annelie Mollbrink, Joseph Bergenstr hle, et al. Multimodal analysis of composition and spatial architecture in human squamous cell carcinoma. *Cell*, 182(2):497–514, 2020.
3. Amanda Janesick, Robert Shelansky, Andrew D Gottscho, Florian Wagner, Stephen R Williams, Morgane Rouault, Ghezel Beliakoff, Carolyn A Morrison, Michelli F Oliveira, Jordan T Sicherman, et al. High resolution mapping of the tumor microenvironment using integrated single-cell, spatial and in situ analysis. *Nature Communications*, 14(1):8353–8368, 2023.
4. Sunny Z Wu, Ghamdan Al-Eryani, Daniel Lee Roden, Simon Junankar, Kate Harvey, Alma Andersson, Aatish Thennavan, Chenfei Wang, James R Torpy, Nenad Bartonicek, et al. A single-cell and spatially resolved atlas of human breast cancers. *Nature Genetics*, 53(9):1334–1347, 2021.
5. Bryan He, Ludvig Bergenstr hle, Linnea Stenbeck, Abubakar Abid, Alma Andersson,  ke Borg, Jonas Maaskola, Joakim Lundeberg, and James Zou. Integrating spatial gene expression and breast tumour morphology via deep learning. *Nature Biomedical Engineering*, 4(8):827–834, 2020.
6. Yuansong Zeng, Zhuoyi Wei, Weijiang Yu, Rui Yin, Yuchen Yuan, Bingling Li, Zhonghui Tang, Yutong Lu, and Yuedong Yang. Spatial transcriptomics prediction from histology jointly through transformer and graph neural networks. *Briefings in Bioinformatics*, 23(5):297–309, 2022.
7. Yuran Jia, Junliang Liu, Li Chen, Tianyi Zhao, and Yadong Wang. THItGene: a deep learning method for predicting spatial transcriptomics from histological images. *Briefings in Bioinformatics*, 25(1):464–474, 2024.
8. Ronald Xie, Kuan Pang, et al. Spatially resolved gene expression prediction from histology images via bi-modal contrastive learning. In *Advances in Neural Information Processing Systems*, pages 1–12, 2024.
9. Ashish Vaswani, Noam Shazeer, Niki Parmar, Jakob Uszkoreit, Llion Jones, Aidan N Gomez, Lukasz Kaiser, and Illia Polosukhin. Attention is all you need. In *Advances in neural information processing systems*, pages 1–15, 2017.
10. Hongzhi Wen, Wenzhuo Tang, Wei Jin, Jiayuan Ding, et al. Single cells are spatial tokens: Transformers for spatial transcriptomic data imputation. *arXiv preprint arXiv:2302.03038*, 2023.
11. Alexey Dosovitskiy, Lucas Beyer, Alexander Kolesnikov, Dirk Weissenborn, Xiaohua Zhai, Thomas Unterthiner, Mostafa Dehghani, Matthias Minderer, Georg Heigold, Sylvain Gelly, Jakob Uszkoreit, and Neil Houlsby. An image is worth 16x16 words: Transformers for image recognition at scale. In *International Conference on Learning Representations*, pages 1–22, 2021.